LRP 622/98 December 1998

Papers Presented at the
17th IAEA Fusion Energy Conference

Yokohama, Japan, 19-24 October 1998

LIST OF CONTENTS

ENERGY CONFINEMENT AND MHD ACTIVITY IN SHAPED TCV PLASMAS WITH LOCALISED ELECTRON CYCLOTRON HEATING

A. POCHELON, S. ALBERTI, C. ANGIONI, S. BARRY, R. BEHN, P. BLANCHARD, P. BOSSHARD, R. CHAVAN, S. CODA, B.P. DUVAL, D. FASEL, A. FAVRE, S. FRANKE, I. FURNO, T.P. GOODMAN, P. GORGERAT, M. HENDERSON, F. HOFMANN, J-P. HOGGE, P-F. ISOZ, B. JOYE, J.B. LISTER, X. LLOBET, J-C. MAGNIN, P. MANDRIN, A. MANINI, B. MARLETAZ, Ph. MARMILLOD, Y. MARTIN, J-M. MAYOR, J. MLYNAR, J-M. MORET, Ch. NIESWAND, P.J. PARIS, A. PEREZ, Z.A. PIETRZYK, R.A. PITTS, A. REFKE, H. REIMERDES, J. ROMMERS, O. SAUTER, W. VAN TOLEDO, G. TONETTI, M.Q. TRAN, F. TROYON, P. VYAS, H. WEISEN
Centre de Recherches en Physique des Plasmas,
Association EURATOM - Confédération Suisse
Ecole Polytechnique Fédérale de Lausanne
CH-1015 Lausanne, Switzerland

Y.V. ESIPCHUCK, N. KIRNEVA, A.A. MARTYNOV, K.A. RAZUMOVA, A. SUSHKOV
Institute of Nuclear Fusion, Russian Research Centre,
Kurchatov Institute
123 182 Moscow, Russia

F. PORCELLI, E. ROSSI
Dipartimento Di Energetica
Politecnico di Torino
I-10129 Torino, Italy

Abstract

Confinement in TCV (Tokamak à Configuration Variable) EC heated discharges is studied as a function of plasma shape, i.e. as a function of elongation $1.1 < \kappa < 2.15$ and triangularity $-0.65 \leq \delta \leq 0.5$. The electron energy confinement time is found to increase with elongation, in part due to the increase of plasma current with elongation. The beneficial effect of negative triangularities is most effective at low power and tends to reduce at the higher powers used.

The large variety of sawtooth types observed in TCV for different power deposition locations from on axis to the q=1 region can be simulated with a model including a local power deposition, a growing m/n=1 island (convection and reconnection), plasma rotation and finite heat diffusivity across flux surfaces.

1. INTRODUCTION

The improvement in tokamak performance over the last 25 years is not only due to the fact that tokamaks have grown in size, but is also a result of modifications of the basic tokamak concept. The evolution from circular to noncircular cross sections and, in particular, the vertical elongation of the plasma cross section κ allows for higher plasma current, since the maximum current scales as $I_p \sim (1+\kappa^2)/2$.

Increasing the plasma current offers two advantages. The first advantage is that the global energy confinement time increases with current, according to several widely used scaling laws [1, 2]. The second advantage is that vertically elongated and D-shaped cross sections allow much higher normalised pressures, i.e. β values, than circular ones [3, 4]. The β-limit, determined from numerical MHD stability analysis [4], $\beta(\%) = c_T I_p(\mathrm{MA})/[a(\mathrm{m})B(\mathrm{T})]$, scales with the plasma current I_P; a is the minor radius, B the toroidal magnetic field, and c_T is the Troyon factor, which is typically between 2.5 and 4.0, depending on the pressure and current profiles. The good agreement of ideal β-limit calculations in highly elongated plasmas with experiment [5, 6] strongly suggests to increase the design κ in ITER.

Electron Cyclotron Heating [7, 8] (ECH) experiments on TCV (achieved parameters: R=0.89m, a=0.25m, κ=2.58, $-0.7<\delta<0.9$, I_p=1MA, B=1.43T) are presently aimed at the study of the confinement properties of variably shaped plasmas. For these studies, an ECH power of 1.4 MW is injected at the second harmonic, 82.7GHz. This power level is already an order of magnitude larger than the Ohmic power during ECH, but represents only a third of the planned

total power (3MW at the second harmonic and 1.5MW at the third harmonic, 118 GHz). EC heating has been chosen for TCV, to cope with the large variety of plasma shapes. Each 0.5 MW gyrotron is connected to a steerable launcher, which can be moved during a tokamak discharge. A universal polariser is included in each transmission line to provide the polarisation needed at the plasma boundary for optimal power coupling.

A number of improvements have been made to the first wall graphite protection during the 1997 shutdown. Surface coverage has been increased from ~60% to ~90% by addition of new tiles on previously exposed areas on the low field side wall. These new elements now allow for heating of negative triangularity discharges. The central column tiles have been completely redesigned and have now a toroidal profile optimised for high power experiments. The wall is boronised regularly.

2. CONFINEMENT AS A FUNCTION OF PLASMA SHAPE

2.1 Confinement study: definition and parameter range

The aim is to study confinement as a function of elongation κ, ($1.1 < \kappa < 2.15$), and triangularity δ, ($-0.65<\delta<0.55$). Two values of q_{eng} ($q_{eng}=5abB/RI_p$), 1.7 and 3 are used, ($2.3<q_a<6$; $0.2<I_p<0.7$MA). The engineering safety factor q_{eng} is used instead of the usual q_a to parametrise the plasma current since constant q_{eng} results in similar normalised profiles independent of the plasma shape [9]. The standard central density n_{eo} is ~2-2.5×10^{19} m^{-3}, while the influence of density is only studied for a restricted number of shapes. All discharges are limited L-mode discharges. Up to 1.4 MW ECRH was injected, with the power deposition region located near the magnetic axis, largely inside the sawtooth inversion radius. At higher q_{eng}, due to finite beam width and shrinking of the q=1 surface, together with a smaller paramagnetic resonance shift at lower current, the beam moves somewhat off-axis, but is still well inside the q=1 radius. Thus, we have always central power deposition conditions.

Three gyrotrons were used for this study, two of them launching from the upper lateral ports and one from the equatorial port. The power was raised to its maximum value in three steps of typically 0.2 s duration. Confinement data are used after the establishment of a constant soft X-ray flux, which led to the exclusion of a 40-50 ms transient period at the start of each power step. Between the 2nd and 3rd step the power was modulated during 0.2 s. The power deposition location was obtained from soft X-rays at the EC shut-off, from power modulation experiments, and qualitatively from the sawtooth shapes (see section 3.1).

The EC power, P_{EC}, is measured near the torus calorimetrically between discharges. The gyrotron power can be set within 5% and is indeterminate to ±10%. The elliptical polarisation of the X2-beam is adjusted to maximise the power coupling at the plasma boundary for all geometries. In most of the cases studied, the power coupled to the X-mode was calculated as greater than 98%.

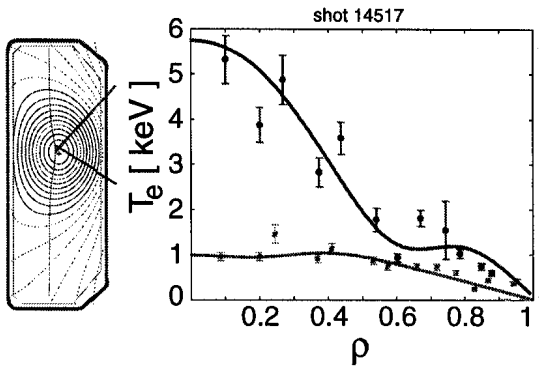

FIG. 1. Thomson electron temperature profile for κ=1.5, δ=0.2, $n_{eo}=1.3\times10^{19}m^{-3}$ during Ohmic and ECRH (1.4 MW). The central deposition aimed with upper lateral and equatorial launchers is indicated.

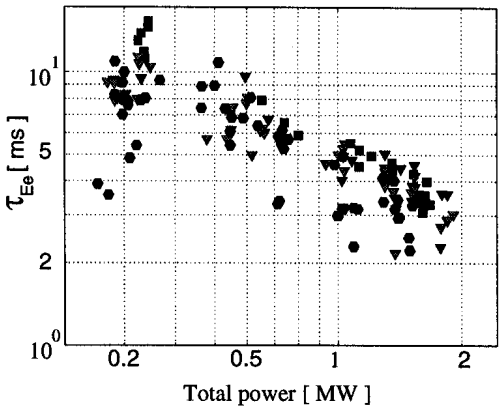

FIG. 2. Electron confinement time versus total power for κ=1.5, δ=0.2 (squares: $n_{eo19}>3$, triangles: $2<n_{eo19}<3$, hexagons: $n_{eo19}<2$).

The electron energy content W_{Ee} is obtained from Thomson scattering measurements, taken every 17 ms. The T_e and n_e profiles, measured along a vertical chord (at R=0.9m), are projected onto normalised flux co-ordinates and fitted with cubic splines. Therefore the calculation of W_{Ee} depends on the equilibrium reconstruction and on the profile fits. This procedure is straightforward for positive triangularity and low elongation discharges, where MHD mode activity is low, as shown in Fig. 1. For negative triangularity and high elongation, the profiles show occasionally large fluctuations within the sawtooth inversion radius, which can make the fitting procedure problematic. Such shots were rejected from the database. The electron energy sometimes fluctuates strongly in time owing to large sawtooth relaxations at positive triangularity and with 1.4 MW of ECRH. Typically ten Thomson profiles were available after the exclusion of the initial transient period at the beginning of each step. These multiple profiles were averaged to reduce the influence of fluctuations.

Typical values of the effective charge Z_{eff}, calculated from soft X-ray flux (dominated by carbon emission) and Thomson temperatures, are $Z_{eff} \geq 4$ during the Ohmic and ECRH phases. Ion temperatures from neutral particle analysis range from 200 to 250 eV. Therefore the ion contribution to the total energy is negligible.

2.2 MHD activity

MHD activity does not only influence the T_e profile reconstruction but can also degrade the confinement itself. In particular for $\delta < -0.2$ the m/n=2/1 mode has been frequently observed during phases with and without auxiliary heating power and irrespective of the edge safety factor.

Sawteeth were present in a wide range of the investigated plasma shapes. Ohmic sawteeth, at κ=1.5, δ=0.2 and typical densities of 2-3×10^{19}m^{-3} have a period $\tau_{ST} \sim 2$ ms. Their period and size increase with triangularity up to $\tau_{ST} \sim 3$ ms and up to a relative crash amplitude, observed with a soft X-ray diode viewing the plasma core ($I_{SX\text{-}R}$), of 20%. For negative δ the relative crash amplitude decreases down to a few % and can disappear within the resolution limit [10]. The crash amplitude as well as the sawtooth period decrease with elongation. Occasionally, no sawteeth have been observed in discharges with $\kappa > 2$.

With ECH deposition within the q=1 surface, different forms of sawteeth have been observed, ranging from normal triangular sawteeth for on-axis deposition to saturated and inverted sawteeth for deposition closer to the inversion radius. For q_{eng}=2, κ=1.55, δ=0.25, the observed sawtooth shapes change with increasing heating power from normal to saturated to inverted sawteeth. For higher q_{eng}=3, saturated sawteeth already appear at lower heating power, indicating that the actual deposition was somewhat off-axis (see section 3.1.1).

The effect of power on sawtooth period and size depends on triangularity: for instance at κ~1.5, for δ>0.2 and low q_{eng} to ensure central deposition, the sawtooth period and crash amplitude increase with increasing heating power up to $\tau_{ST} \sim 5$ ms and up to a relative crash amplitude of 35%, whereas for δ<0.2 the sawtooth period decreases with increasing heating power.

2.3 Scaling of electron energy confinement time

The dependence of the electron energy confinement time on total power and density was studied over a wide power range in the centre of the (κ,δ) scan (κ=1.5, δ=0.2), as shown in Fig. 2. The electron energy confinement time is clearly seen to decrease with power and to increase with density.

In an attempt to obtain a simple general power law to describe the dependence of τ_{Ee} on n_e, P, κ, δ and I_p, we have applied a multi-variable regression to the database. The dependences on κ and I_p cannot be separately determined, owing to the strong correlation between these quantities in our data set. The power law we are able to express so far must therefore contain a free parameter, as follows:

$$\tau_{Ee}[\mathrm{ms}] = 1.9 \times 6.5^{\alpha_I}\, n_{e\_av19}{}^{\alpha_n}\, P^{\alpha_P}\, I_p^{\alpha_I}\, \kappa^{\alpha_\kappa}\, (1+\delta)^{\alpha_\delta}\ [\mathrm{m}^{-3}, \mathrm{MW}, \mathrm{MA}], \qquad (1)$$

where α_n=0.45±0.2, α_P=-0.75±0.1, α_δ=-0.35±0.3, α_κ=1.5(1-α_I)±0.4 and α_I remains undetermined. These uncertainties result from a 25% error on τ_{Ee}. Good fits are obtained with α_I in the range $0 \leq \alpha_I \leq 0.7$, as illustrated in Fig. 3 for the case α_I= 0.5.

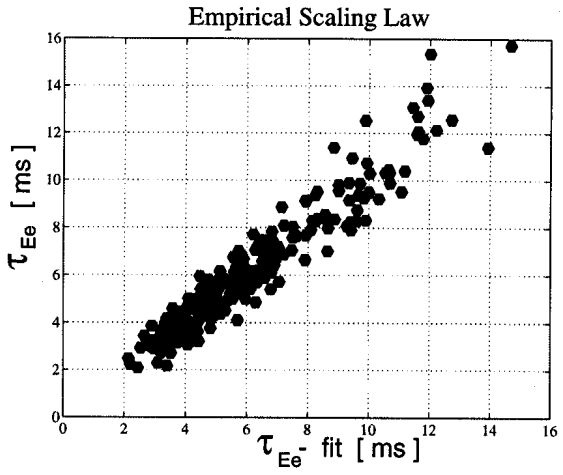

FIG. 3. Empirical scaling law for TCV ECRH data set, see equation (1).

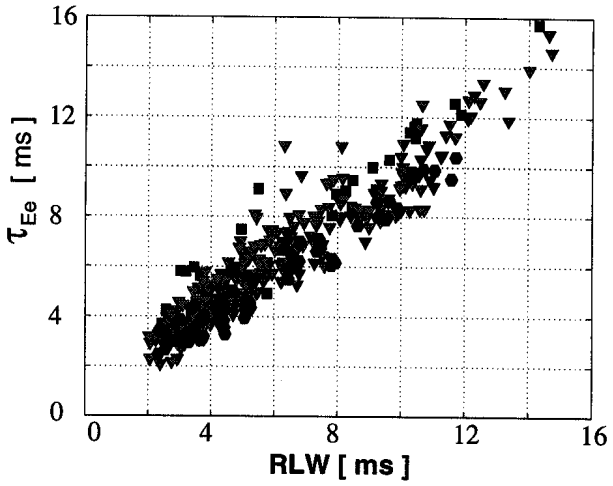

FIG. 4. Fit to Rebut-Lallia-Watkins scaling law. The triangularity is not in the RLW scaling. Negative δ appear favourable (squares: $\delta<0$, triangles: $0<\delta<0.3$, hexagons: $\delta>0.3$).

Naturally, such a general scaling, being based on the entire data set, may overlook more detailed effects in particular regions of the parameter space. For instance, power degradation can be calculated for each discharge separately, using the different power steps. This shows that the power degradation increases with density. Also, the beneficial effect of low triangularity or slightly negative triangularity appears to be stronger at low total power.

Most of the improvement with shape in Ohmic plasmas had been explained earlier in terms of geometrical effects. The thermal conductivity of ohmic plasmas was found to be independent of the shape. This observation, combined with geometrical effects on the temperature gradient and degradation with increasing energy flux, was able to explain the observed variation in the energy confinement time [11].

The TCV data is plotted against the Rebut-Lallia-Watkins confinement scaling [12] for comparison, in Fig. 4, and is seen to fit satisfactorily. Since the RLW scaling contains no triangularity dependence, the data points are subdivided in three triangularity classes, showing the beneficial effect of negative triangularity.

2.4 Transport modelling (PRETOR, ASTRA)

Some of the EC heated discharges have been simulated using the code PRETOR [13]. PRETOR is a predictive time-dependent transport simulation code for tokamaks: it couples a 2-D equilibrium solver with the flux-surface averaged 1-D transport equations to compute the evolution of temperature and density of electrons and ions. The RLW model [12], which is implemented in the code, has been modified, only in its geometrical dependence, to simulate discharges with an edge safety factor larger than 5, as the original model does not allow satisfactory simulations of Ohmic TCV discharges in this domain [14]. The experimental temperature profiles of a single shot in the ohmic phase have been analysed and the heat conductivity has been adjusted to reproduce the experimental behaviour, which implies a relatively large transport at the edge ($\chi_e(\rho=0.8)\sim 2 m^2/s$).

With this model, keeping fixed parameter values in all the transport coefficients, discharges have been simulated in the Ohmic and in the ECH phases. A satisfactory agreement is obtained for the temperature, Fig. 5, and density profiles, the electron thermal energy and confinement time, assuming total absorption for the different ECH powers injected.

Simulating the same discharge with ASTRA, a transport code based on the canonical transport model [15], a model of self-consistent profiles, good agreement is found with temperature profiles and confinement time. With a measured ratio of $P_{rad}/P_{OH}\sim 0.2$, using the radiated power measured from bolometry, one must assume only 90% absorption of injected power. A higher radiation level, around $P_{rad}/P_{OH}\sim 0.3$, would result in full power absorption. Thus our data can satisfactorily be simulated by both transport codes.

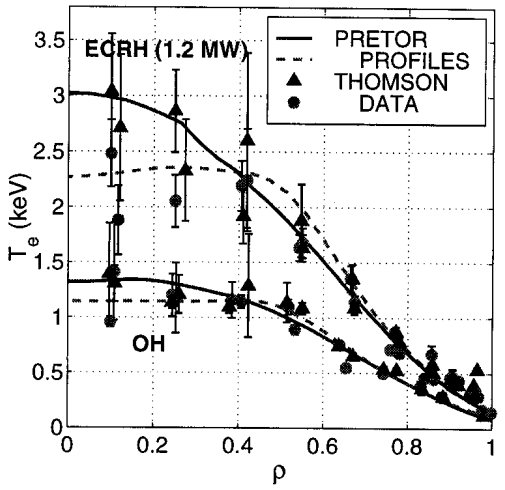

FIG. 5. Comparison between PRETOR temperature profiles and TCV experimental data in Ohmic and ECR heated (1.2 MW) discharges, before (solid line) and after (dashed) sawtooth crash (κ=1.8, δ=0.2, $n_{eo}=2.3\times10^{19}m^{-3}$, q~5).

3. SIMULATION OF CENTRAL RELAXATIONS WITH LOCALISED POWER DEPOSITION

3.1 Central relaxation shape modelling

3.1.1 Experimental description

Non-standard sawtooth traces have been observed in TCV during intense localised EC heating [16]. Fig. 6 shows a sequence of soft X-ray traces obtained while varying the ECH deposition radius. With on axis deposition, standard, i.e. triangular, sawteeth are observed. However, as the ECH absorption region is moved off-axis, the soft X-ray traces change their shape: partially saturated and saturated sawteeth are observed when the heating is still within the q=1 radius. Interestingly, the precursor oscillations that precede the fast relaxation phase of a saturated sawtooth sometimes double their frequency. Humpback sawteeth, first reported by the T-10 team [17], are observed in TCV when the heat is deposited close to the inversion radius. For slightly larger deposition radii, the soft X-ray traces acquire hill-like shapes of low amplitude. Another intriguing experimental observation concerns the optimal deposition radius for obtaining high central temperatures: this radius appears to be close to the q=1 radius. In fact, the sawtooth or humpback period is longest in this case, and the confinement time is at least as large as for central deposition.

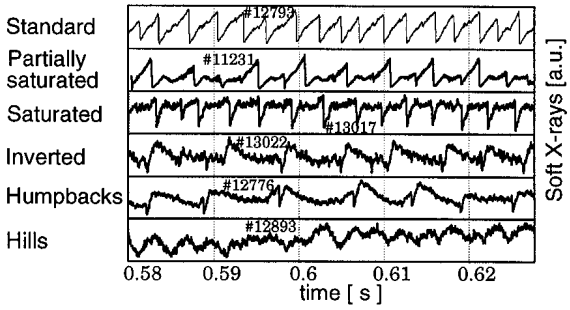

FIG. 6. Standard sequence of central relaxations. Standard sawteeth are produced by on axis power deposition, humpbacks and hills by deposition close to sawtooth inversion radius.

3.1.2 Model of a growing island under localised heating and diffusion

A theoretical model has been recently developed, which accounts for many of the observed features [18] as a function of the heating deposition region. The model is based on the combined effects of m/n=1 magnetic island dynamics, localised EC heating, finite heat diffusivity across the magnetic field lines and plasma rotation. According to this model, the flux surfaces acquire a distinct m/n=1 topology in the plasma central region. The thermal energy distributes uniformly on flux surfaces because of the large (practically infinite) parallel thermal conductivity. Rotation spreads the deposited heat on several flux tubes intersecting the ECH absorption region. Then, the temperature evolution is dominated by heating and perpendicular diffusion (a constant $\chi_\perp$ is assumed) in periods during which the m/n=1 island is either absent or has a stationary width, while convection and mixing due to reconnection become important when the island is growing, the

convection pattern being associated with the specific m/n=1 internal kink mode structure. The model was originally applied to explain the multi-peaked temperature profiles and transport barriers observed in high ECH power density experiments such as RTP [19] and TEXT-U [20]. In this paper, we present two examples which indicate the model ability to reproduce the observed sawtooth shapes in TCV.

In the first example, Fig. 7, a saturated sawtooth is simulated. In this simulation, the heating deposition region is assumed to be between about 2 cm and 4 cm from the equilibrium axis on the high field side; the q=1 radius is at 7 cm. Thus, the heating is off-axis, but is well within the q=1 radius, consistently with the experimental indications. Fig. 7a) shows the simulated temporal trace of the local electron temperature at a distance of about 2 cm from the equilibrium magnetic axis. In Fig. 7b), three temperature profiles at different phases of the saturated sawtooth are shown. These profiles are non-monotonic within the mixing radius, ρ_{mix} and can become rather spiky. In Fig. 7c), a simulated 3D reconstruction of the electron temperature corresponding to the fast relaxation phase at time $t = t_3$ of Fig. 7a) is shown.

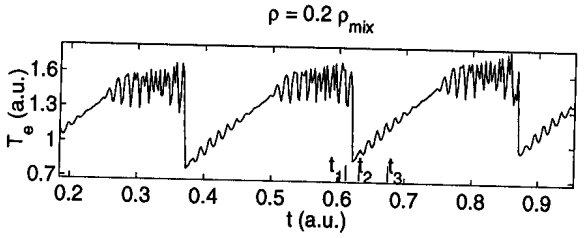

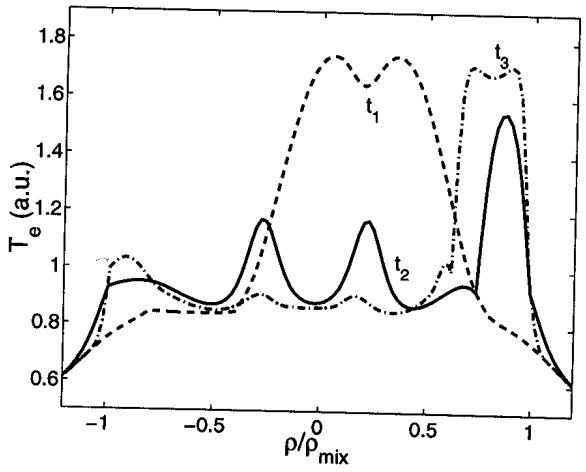

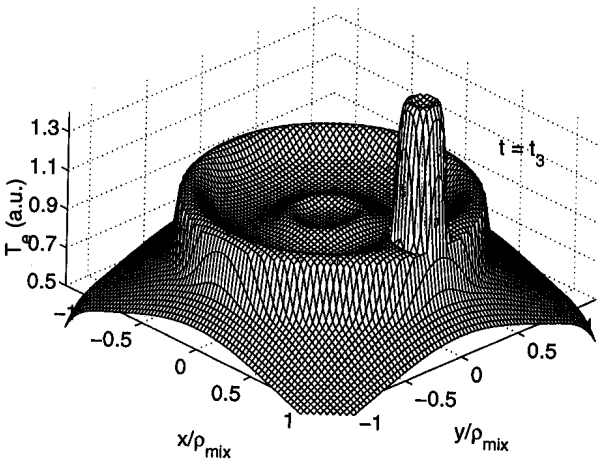

FIG. 7. Simulation of partially saturated sawteeth with power deposition between magnetic axis and the q=1 surface (ρ=0.2ρ_{mix})
7a) temporal evolution of the central temperature. Note the appearance of frequency doubling,
7b) temperature profile before (t_1) and after crash (t_2, t_3), see fig. 7a),
7c) 3D temperature profile at time $t=t_3$, after crash.

In the second example, Fig. 8, we present the simulation of a humpback sawtooth. In order to obtain a humpback from our model, it is important to place the heating region close to the q=1 radius, consistently with the experiment. This produces slightly hollow temperature profiles during the quiescent phase, which then become peaked in the centre as a consequence of the growth of the m=1 island. Fig. 8a) shows the temporal evolution of the central electron temperature. Temperature profiles during the fast relaxation phase are shown in Fig. 8b). Note the relative minimum in the temperature, which deepens with time during the fast phase of the humpback relaxation. Indeed, the characteristic signature corresponding to the sudden drop in temperature between the two humps, visible in Fig. 8a), is related to the fast passage of this relative minimum through the observation point. A 3D reconstruction of the electron temperature is shown in Fig. 8c).

For both simulations, the island width, $w(t)$ is assumed to grow rapidly during the observed, fast relaxation phase. More specifically, for the case of the simulated saturated sawtooth, $w(t)$ grows from 0.4 ρ_{mix} to 1.6 ρ_{mix} in about 200 μs (corresponding to a radial displacement of the original magnetic axis between 0.2 ρ_{mix} and 0.8 ρ_{mix}); for the humpback sawtooth, $w(t)$ grows from practically zero to 1.8 ρ_{mix} in a similar time interval. These values of $w(t)$ are consistent with nearly full reconnection. This behaviour is not predicted theoretically, but it can be inferred from the

experimental data. Nevertheless, the model is applicable as well to cases of partial sawtooth reconnection. The typical radial width of the heat deposition region used in the simulations is between 1 and 2 cm. The results are not particularly sensitive to this width when it varies within this range.

Thus, the model successfully reproduces the shapes of different types of central relaxations as the heating radius is varied, at least qualitatively speaking. In addition, consistently with the experiments, the relative amplitude of the relaxations for central versus off-axis deposition comes out correctly. For example, at constant power injection, high amplitude triangular sawteeth are obtained for on-axis heating, while low amplitude humpback oscillations are obtained when the heating region is close to the q=1 surface.

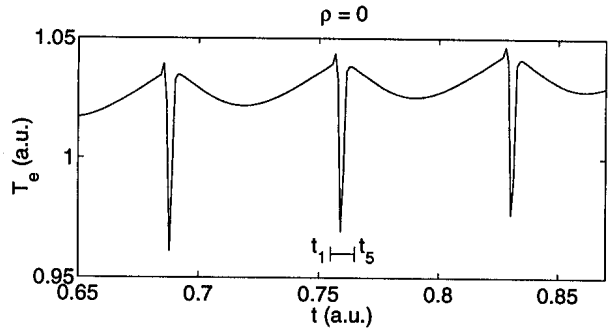

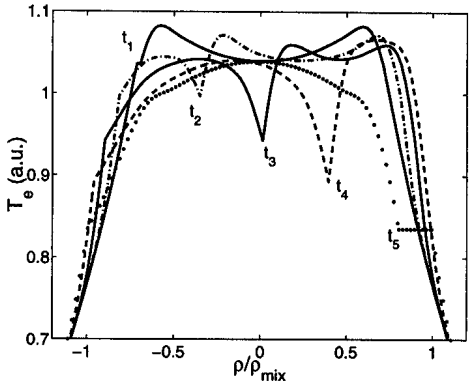

FIG. 8. Simulation of humpback sawteeth with power deposition close to q=1 surface:
8a) temporal evolution of the central temperature,
8b) temperature profile during the fast phase indicated in fig. 8a),
8c) 3D temperature profile in the middle of the crash ($t=t_3$)

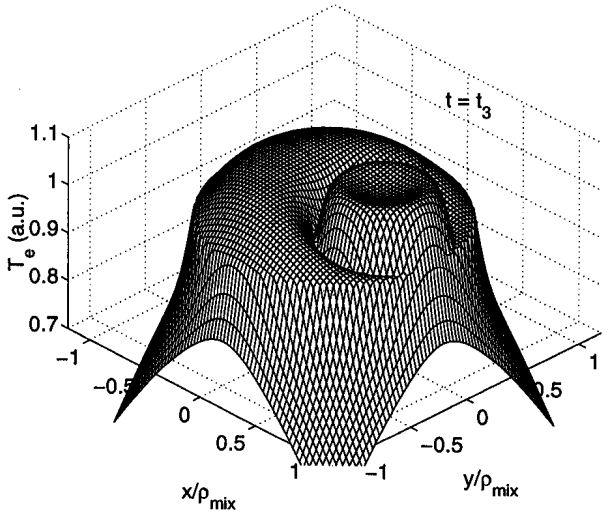

3.2 Sawtooth period simulation with localised power deposition

The transport code PRETOR (see section 2.4), including a sawtooth model developed earlier [21], had been used earlier to simulate sawtooth periods in Ohmic discharges of TCV [22]. It is now used to simulate ECR heated discharges, since it is known that temperature and density profiles are strongly influenced by the presence (or absence) of sawteeth. In particular, the strong dependence of the sawtooth period on power deposition location observed experimentally can also be simulated.

The magnetic shear $s_1 = \rho_1 q'(\rho_1)/q_1$ at q=1 and s_{1crit}, a critical shear above which the resistive internal kink is triggered, define the time at which the sawtooth crash occurs. The sawtooth period depends on the relative time evolution of s_1 and s_{1crit}, and therefore mainly on the local plasma parameters. This explains why the sawtooth activity is very sensitive to ECRH as seen in TCV [16]. Indeed, local heating can change both $s_1(t)$, by changing the local resistive time and the current profile, and $s_{1crit}(t)$ by changing the temperature gradients and confinement time. Moreover, localised deposition affects the q=1 radius both in the transport code and in the experiment, as revealed by measurements of the sawtooth inversion radius. We have simulated a case with 0.5 MW of ECRH deposited over a radial width of 0.15 a. Changing the mean deposition radius from ρ = 0 to 0.3 to 0.5, the code gives ρ_1/a = 0.44, 0.40 and 0.27 respectively. In addition, in the first two cases, s_{1crit} is relatively large, 0.35, because heating inside q=1 gives large gradients at q=1. Therefore long sawtooth periods are obtained, while heating outside ρ_1 gives a very small s_{1crit} and short sawtooth periods. This is in qualitative agreement with the experiment where

sawtooth periods of 2 ms are observed when heating outside q=1 and sawtooth periods increase rapidly to 7-8 ms when heating near the q=1 surface. However, heating closer to the magnetic axis results again in shorter sawtooth period; this indicates that a more detailed simulation including the magnetic topology described above, will be required.

4. CONCLUSIONS

The electron energy confinement has been studied as a function of plasma shape, i.e. as a function of elongation and triangularity in EC heated discharges, with P_{EC} exceeding P_{OH} by up to an order of magnitude. The electron energy confinement improves with elongation. The beneficial effect of low or negative triangularity on confinement, manifested in Ohmic plasmas, is also observed in EC heated plasmas, but tends to decrease with increasing power. Results of transport simulations, using two different models, are found to be consistent with the experimental data.

A variety of different types of central relaxations (sawteeth) are observed when the location of power deposition is moved from the magnetic axis to the q=1 region. The observed sawtooth shapes have been successfully simulated, using a model with localised power deposition, a growing (convection and reconnection) and rotating island at q=1, and finite thermal diffusivity across field lines. Sawtooth shapes similar to those observed in the experiment are reproduced when the power deposition location is moved from the magnetic axis to the q=1 region.

The observation that the sawtooth period is maximum when the power is deposited close to the q=1 surface has also been reproduced by simulation. The model simulates the evolution of the local magnetic shear and includes a critical shear above which the resistive internal kink is triggered.

5. ACKNOWLEDGEMENTS

This work was partly supported by the Fonds National Suisse de la Recherche Scientifique

REFERENCES

[1] CORDEY, J.G. et al., Plasma Phys. Controlled Fusion **39**, B115 (1997).
[2] MARTIN, Y. and SAUTER, O., Considerations on Energy Confinement Time Scalings using present Tokamak Databases and Prediction for ITER Size Experiments, Lausanne Report LRP 616/98.
[3] MILLER, R.L. et al., Phys. Rev. Lett. **43**, (1979) 765.
[4] TROYON, F. et al., Plasma Phys. Controlled Fusion **26**, (1984) 209.
[5] HOFMANN F. et al., Phys. Rev. Lett. **81**, 2918 (1998).
[6] LAZARUS E.A. et al., Phys. Fluids **B 3** (1991) 2220.
[7] GOODMAN T.P. et al., 19th Symp. on Fusion Technology, Lisbon, 1996, Vol I, 565.
[8] GOODMAN T.P. et al., presented by M.Q. TRAN. Invited Paper, 3rd Int. Workshop on Strong Microwaves in Plasmas, Russia, August 1996, ed. by A.G. Litvak, Nizhny Novgorod Univ. Press 1997.
[9] WEISEN H. et al., Plasma Phys. Control. Fusion **40** (1998) 1803.
[10] WEISEN H. et al., Nuclear Fusion **37** (1997) 1741.
[11] MORET, J-M., et al., Phys. Rev. Lett. **79** (1997) 2057.
[12] REBUT P.H., LALLIA P.P. and WATKINS M.L., Proc. 12th Int. Conf. Plasma Physics and Controlled Nuclear Fusion Research, Nice 1988, IAEA Vienna 1989, Vol. 2, 191.
[13] BOUCHER D. and REBUT P.H., in Proc. IAEA Tech. Com. on Advances in Simulation and model. of Thermonuclear plasmas, 1992, Montreal (1993) 142.
[14] ANGIONI C. et al., Proc. of Theory of Fusion Plasmas, Varenna 1998 and LRP 617/98.
[15] DNESTROVSKII Y.N. et al., Plasma Phys. Reports, **23** (1997), (transl. from Fizika Plazmy).
[16] PIETRZYK Z.A. et al., Proc. of Joint ICPP 1998 and 25th EPS, Praha 1998, and LRP 610/98, July 98.
[17] KISLOV D.A. et al., 22nd EPS Conf. on Contr. Fus. and Plasma Phys., Vol. 19C, Part I (1995) 369.
[18] PORCELLI F., ROSSI E. et al., Politecnico di Torino Report, Oct. 1998 PTDE/IN, subm. for publication.
[19] LOPES CARDOZO N.J. et al., Phys. Rev. Lett. **73**, (1994) 256.
[20] CIMA G. et al., Plasma Physics and Controlled Fusion **40** (1998) 1149.
[21] PORCELLI F. et al. Plasma Phys. Contr. Fusion **38** (1996) 2163.
[22] SAUTER O., ANGIONI C. et al., Proc. of Theory of Fusion Plasmas, Varenna 1998 and LRP 617/98.

A PARAMAGNETIC NEARLY ISODYNAMIC COMPACT MAGNETIC CONFINEMENT SYSTEM

W.A. COOPER, J.M. ANTONIETTI
Centre de Recherches en Physique des Plasmas,
Association Euratom-Confédération Suisse,
Ecole Polytechnique Fédérale de Lausanne,
Lausanne,
Switzerland

T.N. TODD
UKAEA Fusion, Culham Science Centre,
UKAEA/Euratom Fusion Association,
Abingdon, Oxon,
United Kingdom

Abstract

A coreless compact magnetic confinement system that consists of sets of helical windings and vertical magnetic field coils is investigated. The helical coils produce a small toroidal translation of the magnetic field lines and seed paramagnetism. The force-free component of the toroidal current strongly enhances the paramagnetism such that isodynamic conditions near the plasma centre can be approached. At $\beta \sim 5\%$, the configuration is stable to local MHD modes. Global MHD modes limit the toroidal current $2\pi J$ to about $-60kA$ for peaked J. Bootstrap-like hollow current profiles generate quasiaxisymmetric systems that require a close fitting conducting shell to satisfy external kink stability.

1. INTRODUCTION

The magnetohydrodynamic (MHD) equilibrium and stability properties of the Sphellamak concept [1] are investigated. The configuration is characterised by a combination of 10 helical coils wound on a sphere of $1m.$ radius, has no central conductor and has a set of vertical field (VF) coils. A model with 4 filaments per coil is shown in Fig. 1a. The helical coils extend to a latitude of 60° and are connected by circular arcs. They are modular with the currents flowing up a helical segment, across the upper connecting arc, then down the adjacent helical segment and then back across the lower connecting arc. This corresponds to a stellarator arrangement of the coil current flow. Part of the current in the inner vertical field coils compensates the current in the connecting segments of the helical coils. The helical coils cause a toroidal translation of the magnetic field lines and assist in providing a seed paramagnetism. Similar coils sets previously proposed [2-4] did not explore the potential to seed paramagnetism, to improve confinement properties and to study MHD stability. A toroidal plasma current, nevertheless, must be driven in this device. The force-free current that it produces generates the toroidal (and poloidal) magnetic flux that guarantees the formation of flux surfaces and the confinement of the plasma. Furthermore, the current enhances the paramagnetic effect very strongly. A previous investigation has modelled the plasma current with fixed toroidal filaments and field line tracing studies have been applied to investigate the configurational properties of the system [1]. In this work, we apply the free boundary version of the three dimensional (3D) VMEC equilibrium code [5] using a distributed toroidal plasma current to obtain MHD equilibria that model the device. The local stability modules of the TERPSICHORE

code [6] are applied to determine the Mercier criterion and the ideal ballooning stability characteristics of the equilibria. The global stability modules of this code are used to determine the stability with respect to internal and external kink modes.

2. MHD EQUILIBRIUM AND STABILITY

The parameters that have been investigated correspond to a current of $300kA$ in the helical coils ($75kA$ per filament), while the upper VF coil carries $-150kA$, the lower VF coil carries $+150kA$ and the outer VF coils have $-20kA$. The plasma current is varied from $-50kA$ to $-550kA$ with a peaked profile. The pressure, inverse rotational transform and differential volume profiles for a case with $-200kA$ and volume averaged $\beta = 2\mu_0 \int d^3xp / \int d^3xB^2 = 5.2\%$ is shown in Fig. 1b. The pressure profile is prescribed as $p(s) = p(0)[250(1-s^2)^2 + 5(1-s)]/255$ and the toroidal current profile is prescribed as $2\pi J'(s) = 0.5\pi J'(0)[3(1-s)^5 + (1-s^5)^2]$, where the symbol $'$ indicates a derivative with respect to s, where $0 \leq s \leq 1$ constitutes the radial variable proportional to the toroidal magnetic flux (plasma volume enclosed). The total toroidal plasma current is $2\pi J(1)$. The mod-B distribution on the cross sections at the beginning of the period and at half period are displayed in Fig. 2. The magnetic field has a maximum value of $1/3T$ at the magnetic axis and is much smaller towards the edge of the plasma. In the central region of the plasma, the mod-B contours align closely with the flux surfaces. They diverge towards the plasma boundary. The equilibrium state thus is nearly isodynamic [7]. In stellarator configurations, the curvature of the magnetic axis precludes the strict existence of isodynamicity. In our case, the plasma current induces a strong paramagnetic effect which produces the isodynamic conditions near the axis. However, this condition does not hold close to the plasma edge. Consequently, the configuration can be more closely associated with quasi-isodynamic [8] or pseudosymmetric [9] systems. The strong paramagnetism in the bulk of the plasma also produces a magnetic hill. This is not particularly favourable for MHD stability. The ballooning modes are stable and the Mercier modes are only unstable very locally near mode rational surfaces at $\beta \sim 5\%$ as shown in Fig. 3a. The Mercier criterion is marginally stable at midvolume and is more restrictive than localised ballooning modes. A further increase in β could be realised because there is room to increase the pressure gradient in the outer 1/3 fraction of the plasma volume and still remain stable to local modes. The large global magnetic shear generated with peaked current profiles constitutes an important stabilising mechanism for local MHD modes for $\beta < 6\%$. External $m/n = 1/1$ and internal $m/n = 1/3$ limit the toroidal plasma current to about -60 to $-70kA$. It must be noted that this limit is extrapolated from unstable configurations with higher current and that we have been unable to converge an equilibrium state when the current is smaller than $-90kA$. This could possibly indicate an equilibrium limit at low toroidal current, but has yet to be confirmed because we have calculated equilibria with broader current profiles at $-50kA$ and lower β. The configuration is clearly three dimensional for the parameters we have chosen. For the broader current profile cases we have investigated, the main effect of reducing the toroidal current to $-50kA$ (keeping the vertical field fixed) is to shift the plasma inwards away from the helical coils. The helical modulation becomes very weak and the system becomes practically axisymmetric. This configuration retains its strong paramagnetic character with the mod-B contours closely aligned with the flux surfaces near the central region. The plasma volume and cross section become smaller and the rotational transform increases.

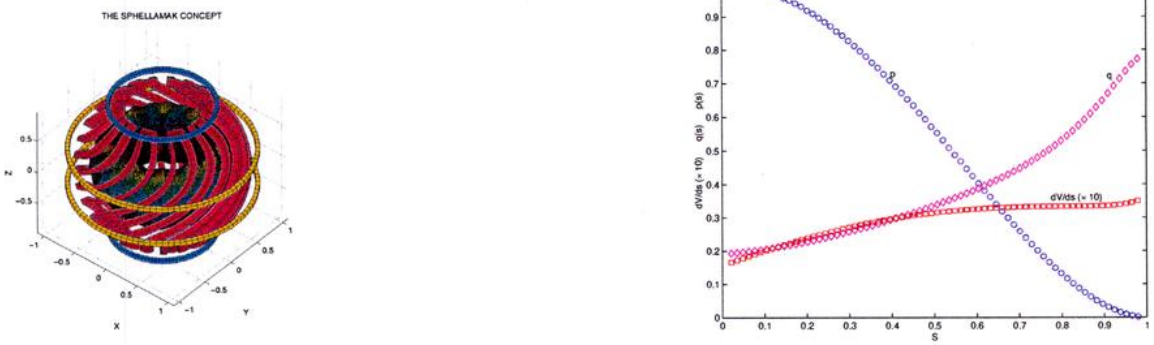

Fig. 1a. (left) The coil system of the Sphellamak configuration. There are 10 helical coils, an inner pair of vertical coils and an outer pair of vertical coils. Fig. 1b. (right) The differential volume (×10), normalised pressure and inverse rotational transform q profiles for a case with $-200kA$ toroidal current and $\beta = 5.24\%$.

Fig. 2. The mod-B distribution in the Sphellamak at the beginning of the period (left) and at half period (right) for a case with $-200kA$ toroidal current and $\beta = 5.24\%$.

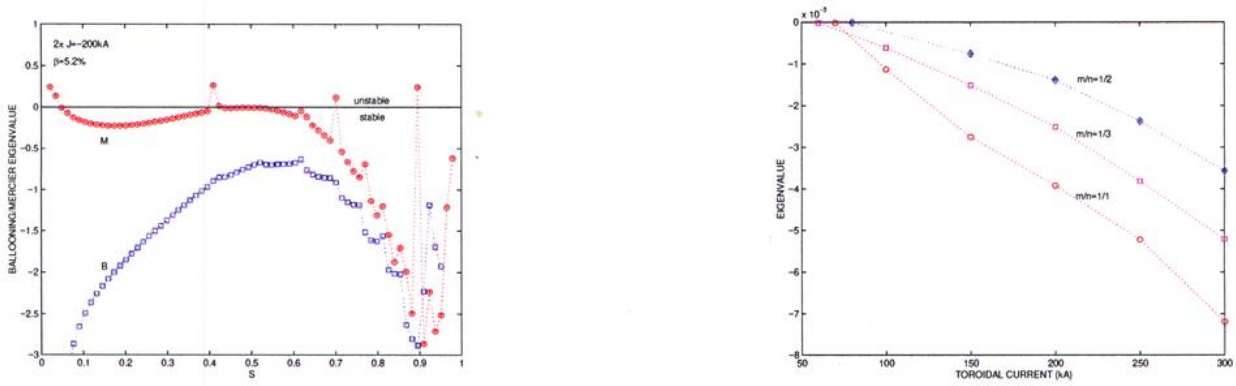

Fig. 3a. (left) The Mercier criterion (circles) and the ballooning eigenvalue (squares) profiles for a case with $-200kA$ peaked toroidal current and $\beta = 5.24\%$. Fig. 3b. (right) The eigenvalues of global modes dominated by the $m/n = 1/1$ (circles), the $m/n = 1/2$ (diamonds) and the $m/n = 1/3$ (squares) components as a function of the toroidal current for a sequence of Sphellamak equilibria with peaked current profiles and $\beta \sim 5\%$. The marginal points have been obtained by extrapolation. Negative eigenvalues indicate stable (unstable) conditions for local (global) MHD modes with the normalisation we have adopted.

The structure of the magnetic field implies that particles can be trapped only towards the plasma edge which localises any bootstrap current drive to that region. To model a bootstrap current, we prescribe a hollow current profile. The configuration under these conditions becomes quasiaxisymmetric. It is stable to Mercier and ballooning modes at $\beta \sim 10\%$ when the pressure profile is modified to have very weak gradients in the regions of vanishing global magnetic shear. However, it requires a tightly fitting conducting wall to stabilise external $m/n = 1/1$ kink modes with a toroidal current of $-400kA$. We have also considered a case with a mildly hollow current profile where we have changed the direction of the current in the helical coils so that the contribution of these coils to the rotational transform is opposite that of the plasma current. With a toroidal current of $-150kA$ and a tailored pressure profile to guarantee local MHD mode stability at $\beta \sim 5\%$, a close fitting conducting wall is also required to satisfy stability. This case is quasiaxisymmetric.

3. DISCUSSION AND CONCLUSIONS

The Sphellamak concept that relies on the toroidal plasma current to generate the toroidal magnetic field displays an extremely strong paramagnetic effect without requiring dynamo action. This results in a system that is nearly isodynamic, at least near the centre of the plasma. The resulting transport properties could approach classical levels making it a potentially very attractive system. A large fraction of the confining magnetic fields are produced from the force-free currents rather from external coils. Consequently, the values of β we have reported are significantly larger with other more conventional definitions of this parameter. If we replace the volume averaged magnetic energy density in the definition we adopt for β with the magnetic energy density from the vacuum fields only at the centre of last close flux surface, the value of β would exceed 500%. Global kink modes limit the maximum toroidal current that can be achieved in these configurations. A close fitting conducting wall is required with hollow toroidal currents that model the bootstrap effect. With peaked toroidal current, marginal stability with respect to kink modes with a conducting wall far from the plasma is satisfied for values of current $(-60kA)$ where the computation of equilibria with the VMEC code has had difficulty to yield a converged solution so far.

Acknowledgement

We are greatly indebted to Dr. S. P. Hirshman for providing us the 3D VMEC equilibrium code to perform part of this work. This work was supported by the Fonds National Suisse pour la Recherche Scientifique and by Euratom.

References

[1] TODD, T.N. Proc. Spherical Tokamak Workshop, St. Petersburg, Russia (1997).

[2] FURTH, H.P., HARTMAN, C.W., Phys. Fluids **11** (1968) 408.

[3] HARTMAN, C.W., US-Japan Joint Symp. on Compact Torus and Energetic Particle Injection, PPPL, (1979)

[4] MOROZ, P.E., Phys. Lett **A236** (1997) 79.

[5] HIRSHMAN, S.P., BETANCOURT, O., J. Comput. Physics **96** (1991) 99.

[6] COOPER, W.A., Plasma Phys. Contr. Fusion **34** (1992) 1011.

[7] PALUMBO, D., Nuovo Cimento **B53** (1968) 507.

[8] NUEHRENBERG, J., ZILLE R., in Theory of Fusion Plasmas, Editrice Compositori, Bologna (1997).

[9] SHAFRANOV, V.D., MIKHAILOV, M.I., SKOVORODA, A.A., SUBBOTIN, A.A., "Pseudosymmetric Magnetic Confinement Systems", Int. Symp. on Plasma Dynamics in Complex EM Fields, Kyoto, 1997.

DIRECT MEASUREMENT OF THE PLASMA EQUILIBRIUM RESPONSE TO POLOIDAL FIELD CHANGES AND H_∞ CONTROLLER TESTS IN TCV

J.B. LISTER[1], R. ALBANESE[2], G. AMBROSINO[3], M. ARIOLA[3], I. BANDYOPADHYAY[4], A. COUTLIS[5], D.J.N. LIMEBEER[5], A. PIRONTI[3], F. VILLONE[6], P. VYAS[1], J.P. WAINWRIGHT[5]

1) Centre de Recherches en Physique des Plasmas, Association Euratom-Confédération Suisse, Ecole Polytechnique Fédérale de Lausanne, CH-1015 Lausanne, Switzerland
2) Associazione Euratom/ENEA/CREATE, Dipartimento di Ingegneria, Università degli Studi di Napoli Federico II, Via Claudio 21, I-80125 Napoli, Italy
3) Associazione Euratom/ENEA/CREATE, Dipartimento di Informatica e Sistemistica, Università degli Studi di Napoli Federico II, Via Claudio 21, I-80125 Napoli, Italy
4) Institute for Plasma Research, Bhat, Gandhinagar 382428, India
5) Centre for Process Engineering, Imperial College of Science, Technology and Medicine, Roderic Hill Building, London SW7 2BZ, United Kingdom
6) Associazione Euratom/ENEA/CREATE, Dipartimento di Ingegneria Industriale, Università di Cassino, I-03043, Cassino (Fr), Italy

Abstract

The control of ITER provides several challenges which can be met using existing techniques for the design of modern controllers. The specific case of the control of the Poloidal Field (PF) system has sollicited considerable interest. One feature of the design of such controllers is their dependence on a sufficiently accurate model of the full system under control. To this end, experiments have been performed on the TCV tokamak to validate one plasma equilibrium response model, the CREATE-L model. Using a new technique, the open loop response of TCV has been directly measured in the frequency domain. These experimental results compare well with the CREATE-L model. This model was subsequently used to design a PF system controller, using methods proposed during the ITER EDA and the first test on TCV has been successful.

1. INTRODUCTION

Present tokamaks typically use low order PID controllers. Recently, considerable attention has been focused on the design of plasma position, current and shape controllers for the ITER Poloidal Field (PF) system. The controller is restricted to demand as little power as possible, to limit surges in the total power required for the PF system and to maintain the specified shape in the presence of disturbances. Simulations using modern controllers have provoked a great deal of interest due to their ability to deliver this performance. These design techniques require an accurate model of the tokamak, which is used in a mathematical optimisation to find an optimal controller. There has been some concern that the rather unpredictable nature of a tokamak, together with plasma noise and internal disturbances, might pose problems for these controllers. A long term program was therefore undertaken to validate the full ITER EDA design procedure of such an advanced controller from both modelling and controller design aspects. The TCV tokamak possesses a large number of PF coils, all separately powered, and represents a suitable device for such studies; technical details of TCV control are in [1].

Firstly, we required an accurate model of the TCV tokamak and there are two standard approaches to do this. The most prevalent method for modelling the plasma response has been phenomenological. A mathematical model is constructed from the relevant physical laws with appropriate, but often debated, simplifying assumptions. Benchmarking a linearised deformable plasma equilibrium model, CREATE-L [2] was started with closed loop performance comparisons between the modelled tokamak and experiments on limited discharges [3] and diverted discharges [4] in the presence of external PF coil voltage perturbations. These experiments showed no discrepancies between the model and the experiment. A new circuit equation model of TCV also showed good agreement (RZIP [5]).

The second approach to modelling the plasma response is based on system identification. No *a priori* physics knowledge is assumed. Instead, a fit to experimental data is used to determine a suitable mathematical model. The main features of TCV, that it is unstable with a large number of inputs and a large number of outputs, make identifying TCV a challenge for such techniques. The open loop response cannot be measured by simply opening the feedback loops, since the vertical position of the plasma is unstable once the plasma cross-section is elongated. However the open loop response can be recovered from sufficient closed loop data. These experiments lead directly to an open loop model of the current, shape and position responses at a set of driving frequencies.

These frequency response estimates can be compared directly with open loop plasma response models. This open loop comparison corrects a recognised deficiency in previous model-experiment comparisons of the closed loop behaviour in TCV [3,4]. A feedback system generally tends to reduce the sensitivity of the closed loop system to variations in the open loop plasma response model, whereas the success of a high-performance controller design depends on the accuracy of the open loop model. The effect of the feedback controller is no longer present in our new open loop data and a direct comparison is possible.

Finally, we designed a modern controller and tested its functionality on the TCV tokamak using a fast digital plasma control system [6]. The complete life-cycle of *a priori* modelling, closed loop comparisons, open loop measurements and controller design illustrates that such new techniques can be considered for a future large tokamak.

2. MEASUREMENT OF THE OPEN LOOP RESPONSE

A weakly shaped plasma was chosen since no experience of this type of multivariable identification was available. A low vertical instability growth rate (~200s^{-1}) implied a low open loop bandwidth which was considered to be more suitable for this first attempt. The main parameters were: R=0.87m, a=0.24m, B_ϕ=1.4T, I_p=200kA, k_{95}=1.4, δ_{95}=0.23, q_a=4.6, n_e=2.2×10^{19}m^{-3}.

Point frequency estimates were obtained by exciting the system with a multi-sinusoidal signal with 29 sine waves spanning the angular frequency range 20rad/s to 3000rad/s. The smoothness of the underlying response as a function of frequency is assumed. The period of the slowest sine wave in the excitation signal was designed to be 0.3s, resolvable during the experiments. The highest excitation frequency was designed to be below half the sampling frequency and also above the assumed TCV bandwidth. The excitation signal is injected at point *s* in Fig. 1. The phases of the different frequency components were chosen to minimise the maximum amplitude of the total stimulation waveform. During each identification experiment, the input voltages and the output signals were acquired at 5kHz, over a time interval of 0.5s. The transients following the start of the stimulation were allowed to decay. Any offsets and linear drifts were removed from the signals before analysis.

The test signal was scaled to ensure that it was within the linear range of the power supplies but also large enough to provided sufficient signal-to-noise ratio in the resulting data. The final voltages applied to the PF coils lay within 80% of the power supply limits. If the response is noise-free, linear and time-invariant, the frequencies of the spectral components in the measured signal will match those in the test-signal exactly. The frequency spectrum of the measured signals at these frequencies was obtained by a least squares fit. The amplitudes of the residuals, which cannot be decomposed into the measurement frequencies, are a measure of data corruption due to external disturbances, measurement noise and non-linearities of the system. The smaller the residuals, the greater the confidence in the results of the identification procedure. The residuals in these experiments were small compared with the signals.

The frequency spectra of all of the input and output data collected during the identification experiments was then used to obtain the open loop frequency response. For the j^{th} experiment we define the input frequency spectrum as $U_l^j(\omega_i)$ and the output frequency spectrum as $Y^j(\omega_i)$, where l indexes the inputs. Our estimate of the system frequency response at each measurement frequency is then given by,

$$\hat{G}(\omega_i) = \begin{bmatrix} Y^1(\omega_i) \\ \vdots \\ Y^q(\omega_i) \end{bmatrix}^T \begin{bmatrix} U_1^1(\omega_i) & \cdots & U_q^1(\omega_i) \\ \vdots & \ddots & \vdots \\ U_q^1(\omega_i) & \cdots & U_q^q(\omega_i) \end{bmatrix}^{-1} \qquad (1)$$

The invertibility of the matrix ($\mathbf{U}_i$) at each frequency is a mild assumption that is satisfied if the corresponding matrix for the designed test-signals is invertible. If that is the case, then the experiments performed are said to be independent. Since TCV has 18 separate PF coil voltage inputs, 18 experiments were required. The condition number of the $\mathbf{U}_i$ matrices varied from 3 to 30, with lower values at higher frequencies, and so were easily invertible.

The agreement between the *a priori* models (CREATE-L and RZIP) is excellent for almost all parameters. Three representative results of input-output frequency responses are shown in Fig. 2.

Many responses show a relatively weak dependence on the model and even agree with the plasmaless model (centre row) and these are always accurate. Some cases show a difference between the plasmaless model and the plasma models (upper row) and the plasma models all agree. Only a few cases are sensitive to the plasma model details (lower row). We also developed a "Grey-Box" model allowing only 6 plasma parameters in the RZIP model to be fitted, fixing all the electromagnetic properties of the tokamak with no plasma, The Best Grey Box Model (BGBM) gave a better result than the *a priori* models in only a few cases. The BGBM approach also indicates which parameters of the plasma response model are most accurately determined by the experimental data and are therefore most important for generating an adequately accurate model. Fig. 3 shows the variation of the Grey Box Model agreement as the 6 plasma coefficients are varied, showing that apart from the plasma inductance and the radial force balance (M33 in Fig. 3) the *a priori* model is barely different from the fitted model. This method has therefore allowed us to measure specific elements of the RZIP circuit equation model.

3. CONTROLLER DESIGN AND TEST

We chose the tracking of separate square pulse reference excursions as a suitable test [1], positioning the plasma above the mid-plane. In this case the natural decoupling between the vertical movement and the other 4 control parameters is lost. Since this was the first attempt, a set of relatively conservative design goals were chosen. The controller should:

- stabilise the reference plasma and similar weakly shaped, symmetric, plasmas positioned at the midplane;
- tolerate uncertainties in the PF coil currents with respect to the nominal model;
- be robust to unpredictable behaviour of the PF coil supplies;
- be insensitive to real experimental noise in the estimators;
- have a low closed loop bandwidth for lower power and minimising voltage saturation.

The main design challenge was therefore to demonstrate that the H_∞ controller could function given real conditions in the tokamak operation, not included explicitly in the linearised model. A simple algorithm was used to avoid large transients when switching between the digital implementation of the PID controller and the H_∞ controller. Details of the H_∞ controller design and implementation are found in [7].

The new controller was implemented in the DPCS and shadowed the analogue control system during the operation of a single tokamak discharge, including the switching between PID and H_∞ controllers during the flat top. This open loop verification of the controller and switching algorithms was adequate to believe that the closed loop control would be acceptable. Following this single test discharge, the DPCS was given control of all the PF coils and the first successful closed loop operation of this controller was achieved. Closed loop stability was obtained. The switching produced no visible transient effects on the overall closed loop control. Fig. 4 shows the behaviour of the 5 controlled parameters during this experiment. The decoupling performance is superior to the PID for all responses and all parasitic cross-couplings. The tracking and decoupling benefits of the H_∞ controller have been clearly demonstrated and no unforseen difficulties were encountered. Work will now concentrate on Power Management strategies, saturation strategies and the explicit control of separatrix gaps during the flat-top.

ACKNOWLEDGEMENTS: Three of the authors (AC, MA, FV) acknowledge mobility support from Euratom. The work was partly funded by the fonds national suisse de la recherche scientifique.

REFERENCES

[1] J.B. LISTER et al., Fusion Technology, **32** 321 (1997)
[2] R. ALBANESE and F. VILLONE, Nuclear Fusion, **38**, 723 (1998)
[3] F. VILLONE, P. VYAS, J.B. LISTER and R. ALBANESE, Nuclear Fusion, **37**, 1395 (1997)
[4] P. VYAS, F. VILLONE, J.B. LISTER and R. ALBANESE, Nuclear Fusion, **38**, 1043 (1998)
[5] A. COUTLIS et al., "Measurement of the Open Loop Plasma Equilibrium Response in TCV," Lausanne Report LRP 611/98 (1998)
[6] J.B. LISTER, M.J. DUTCH, P.G. MILNE and R.W. MEANS, IEEE Trans. Nucl. Science, **45**, 2044 (1998)
[7] M.A. ARIOLA et al., "A modern plasma controller tested on the TCV tokamak" Lausanne Report LRP 606/98 (1998)

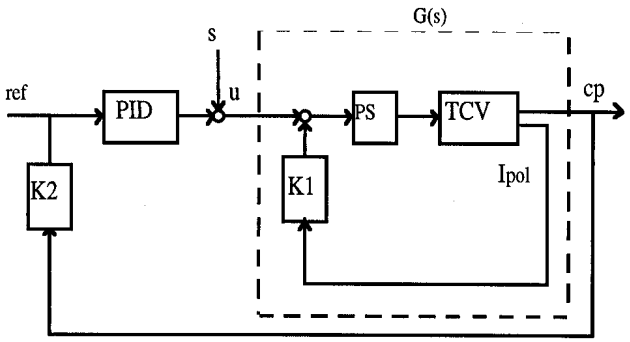

Fig.1 - Schematic of the TCV control loop, showing the power supplies (PS), the tokamak (TCV) and the PF current control loop (K1) as the open loop system G(s), and the controller, comprised by the blocks K2 and PID.

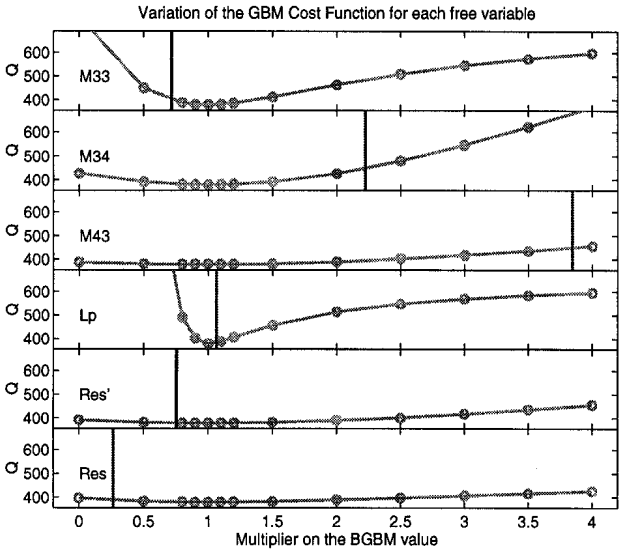

Fig.3 - Open loop results:model cost function sensitivity to the plasma related elements of the RZIP circuit equation model. The most critical elements are the plasma inductance Lp and the Shafranov shift (M33). The nominal model values are shown as vertical bars. When the parameter is critical, the *a priori* estimate is close to the optimum.

Fig.4 - Results of the first experimental test of the H_∞ controller on TCV, indicating good decoupling between the 5 controlled variables. P_VERT controls the radial position, TRI_IN and TRI_OUT control the shape and zIp and Ip control the plasma height and current respectively. The previous PID controller, based on a plasmaless model, showed poor decoupling of some parameters.

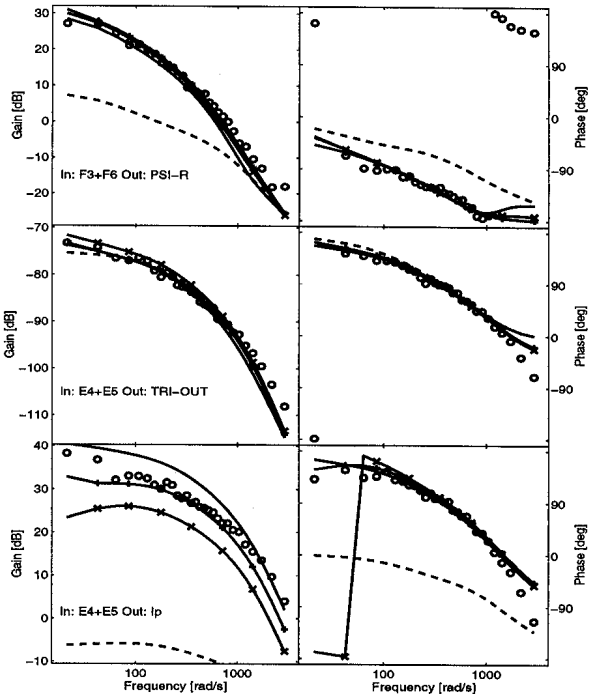

Fig.2 - Frequency responses representing:
a) good agreement between the measured and RZIP and CREATE-L predictions,
b) agreement between the measurements and plasma-less predictions, and
c) BGBM improvement. Measured frequency responses (o), plasma-less model (--), RZIP model (×), CREATE-L (-), and BGBM model (+)

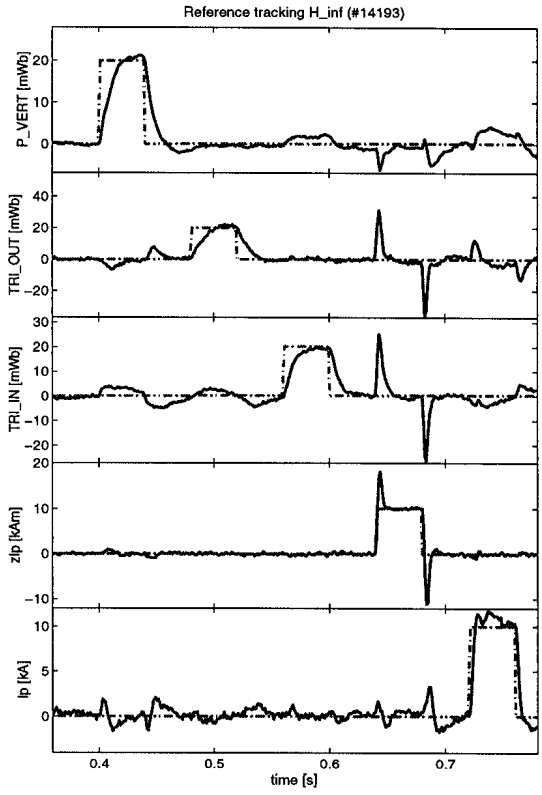

LATEST RESULTS FROM THE ITER H-MODE CONFINEMENT AND THRESHOLD DATA BASES

K. THOMSEN[6], G. BRACCO[5], C. BUSH[8], T.N. CARLSTROM[4], A.N. CHUDNOVSKII[9], J.G. CORDEY[6], J.C. DEBOO[4], S.J. FIELDING[3], T. FUKUDA[7], M. GREENWALD[1], G.T. HOANG[11], A. HUBBARD[1], Y. KAMADA[7], O.J.W.F. KARDAUN[2], S.M. KAYE[8], A. KUS[2], C. LOWRY[6], Y. MARTIN[12], T. MATSUDA[7], Y. MIURA[7], J. ONGENA[10], E. RIGHI[13], F. RYTER[2], D.P. SCHISSEL[4], J.A. SNIPES[1], W. SUTTROP[2], T. TAKIZUKA[7], H. TAMAI[7], K. TSUCHIYA[7], M. VALOVIC[3], ALCATOR C-MOD TEAM[1], ASDEX TEAM[2], ASDEX UPGRADE TEAM[2], COMPASS-D TEAM[3], DIII-D TEAM[4], FTU TEAM[5], JET TEAM[6], JFT-2M TEAM[7], JT-60U TEAM[7], PBX-M TEAM[8], PDX TEAM[8], T-10 TEAM[9], TCV TEAM[12], TEXTOR TEAM[10], TFTR TEAM[8], TORE-SUPRA TEAM[11]

[1]Plasma Fusion Center, MIT, USA
[2]Max-Planck-Institute for Plasma Physics, Garching, Germany
[3]United Kingdom Atomic Energy Authority, Culham, UK
[4]General Atomics, San Diego, USA
[5]ENEA Frascati Energy Research Centre, Frascati, Italy
[6]JET Joint Undertaking, Abingdon, UK
[7]Japan Atomic Energy Research Institute, Naka, Japan
[8]Princeton Plasma physics Laboratory
[9]Russian Research Centre "Kurchatov Institute", Moscow, Russia
[10]ERM/KMS - EURATOM, Belgium State, Belgium
[11]Centre d'Etudes Nucleaires de Cadarache, Cadarache, France
[12]CRPP/EPFL, Lausanne, Switzerland
[13]NET Team, Garching, Germany

Abstract

New H-mode power threshold scaling expressions have been found which incorporates an assumed 1/M isotope dependence for hydrogenic plasmas. Preliminary power threshold predictions using discriminant analysis have also been made. However, the ITER predictions are still uncertain. The log-linear confinement scaling expressions suggest that the L-mode is governed by Bohm type transport, whereas the ELMY H-mode is governed by gyro-Bohm transport. Various non-linear scalings also fit the ELMy H-mode data and a confidence interval for the predicted confinement time in ITER has been established which takes the predictions of these into account.

1. INTRODUCTION

The ITER H-mode Power Threshold, L-mode and H-mode Confinement Databases [1-3] have all been expanded with new data in the last two years and the number of contributing tokamaks has increased. Here some of the recent findings using these databases will be presented, see also [4-6].

2. H-MODE THRESHOLD POWER

The ITER Threshold Database contains data from 10 divertor tokamaks (ASDEX, ASDEX Upgrade, Alcator C-Mod, COMPASS-D, DIII-D, JET, JFT-2M, JT-60U, PBX-M and TCV). Since the previous IAEA conference [7] efforts have been made to understand the causes of the large scatter of the data and to improve the quality of the database by adding new data.

Regressions on the points just at the L-H transition yield the following two expressions (units of M, n_{20}, S, P_{thres}, B, R and a are AMU, 10^{20} m^{-3}, m^2, MW, T, m and m, respectively):

$$P_{thres} = 0.082\ M^{-1.0}\ n_{20}^{0.69}\ B^{0.91}\ S^{0.96}, \qquad \text{RMSE} = 25.2\% \qquad (1)$$

$$P_{thres} = 2.76\ M^{-1.0}\ n_{20}^{0.77}\ B^{0.92}\ R^{1.30}\ a^{0.76}, \qquad \text{RMSE} = 25.1\% \qquad (2)$$

The ASDEX (only circular device), COMPASS-D and TCV (smallest devices with an open divertor) data have not been included in the regressions because their data are above the prediction according to both regression models, see Fig. 1. For the latter 2 devices, neutrals may be the cause of the increased power threshold. Both Eqs. (1) and (2) are dimensionally correct within the uncertainties. The dependence on S is in agreement with the L-H transition being an edge phenomenon. The expressions were determined for pure deuterium. The dependence on M, only valid for hydrogenic plasmas, was imposed based on operation in hydrogen and deuterium as well as tritium [8]. The extrapolated values for ITER using Eqs. (1) and (2), at $n_{20} = 0.5$, are 85 (56 - 153) MW and 107 (63 - 179) MW, respectively. The uncertainty on P_{thres} is largely due to data scatter that can reach a factor of 2 within a single device. The data scatter has several causes that vary from device to device. One effect is wall conditioning, the threshold being higher in high recycling cases. It has been shown in several devices that the edge electron temperature is almost constant for given values of B and I. Therefore, to reach the required temperature, more heating power is necessary at higher edge density (i.e., high recycling). Using the edge density instead of the line-averaged density in the analysis would be preferable. However, the lack of data and the large scatter of the available measurements have prevented a reliable result to be obtained. Moreover, the edge density in ITER is not known with accuracy. Therefore, at present, using the edge density does not improve the prediction. A second cause for scatter in several devices is due to the sawteeth. The heat pulse following a sawtooth crash can trigger the L-H transition when it reaches the edge. Depending on the plasma conditions and time evolution of the discharge, the L-H transition may be triggered by a sawtooth heat pulse with variable efficiency or not at all. Presently, it is not possible to reliably take this effect into account, but modelling is being carried out. A cause of data scatter in Alcator C-Mod is attributed to the variation of the ICRH absorption. Correcting the heating power with experimental absorption factors has decreased the scatter and the density dependence in this device. However, the overall results did not change significantly.

Discriminant Analysis is used to determine a set of hyperplanes in multidimensional space, which best separates two classes of data: one containing the L-mode points, the other the H-mode points. An investigation of power threshold using this approach has been initiated [5]. In order to increase the number of data points all 3 databases (L-mode, H-mode and Threshold database) have been merged together. However, only data from tokamaks contributing to both L-mode and H-mode data have been considered. The resulting dataset is thus significantly different from the one used in the previous section. R, B, κ, q_{95}, n and the loss power P constitute the multidimensional space. The discriminant function (constant on each hyperplane) can be transformed into a function that gives the probability of a data point to belong to the H-mode class. With this model about 75% of the data are well classified. The model can be used to predict the H-mode threshold power in the following way. For design values of R, B, κ, q_{95} and n, the loss power P is increased until the model shows a probability larger than 0.5. That value of P is considered to be the threshold power. The prediction for ITER is 80 (25 - 200) MW. Threshold predictions for independent scans of R, B, κ, q_{95} and n have also been calculated. They show that this model is equivalent to a threshold power scaling which increases with R, B and κ but decreases with q_{95} and n. The latter dependence is not in agreement with the results obtained by regression analysis and hence deserves further consideration.

3. L-MODE CONFINEMENT

The present public L-mode database consists of data from 14 tokamaks (Alcator C-Mod, ASDEX, DIII, DIII-D, FTU, JET, JFT-2M, JT-60U, PBX-M, PDX, TEXTOR, TFTR, Tore-Supra, and T-10). In [4] a dimensionally correct fit to the thermal confinement data for the combined limiter and divertor data subsets is given (in units of s, MA, T, MW, $10^{19}m^{-3}$, AMU, m, -, -):

$$\tau_{th}^{L\text{-mode}} = 0.023\, I^{0.96}\, B^{0.03}\, P^{-0.73}\, n_{19}^{0.40}\, M^{0.20}\, R^{1.83}\, \varepsilon^{-0.06}\, \kappa^{0.64} \qquad (3)$$

The RMSE is 15.8% with no apparent difference between the divertor and limiter data. The scaling predicts 2.1 s L-mode confinement time for ITER. Eq. (3) is equivalent to $\tau_{th}^{L\text{-mode}} \propto \tau_B\, \rho_*^{0.15}\, \beta^{-1.41}\, \nu_*^{0.19}$ and is a Bohm-like scaling.

4. ELMY H-MODE CONFINEMENT

The new public version (DB3v5p) of the ITER H-mode confinement database, ITERH. DB3, was released 1st of June 1998 and is detailed in [4]. This version contains data from 12 different tokamaks: Alcator C-Mod (C-Mod), ASDEX, ASDEX Upgrade (AUG), COMPASS-D, DIII-D, JET, JFT-2M, JT-60U, PBX-M, PDX, TCV and TEXTOR.

This new ELMy H-mode standard dataset (1398 obs. From 11 Tokamaks) [4] is significantly larger than the IAEA 1992 ELMy standard dataset (833 obs. from 6 Tokamaks) [10]. Only 3 correlation coefficients (ρ_{IP}, $\rho_{I\varepsilon}$ and $\rho_{I\kappa}$) are now larger than 0.7 and the principal components have changed significantly. The extrapolation to ITER is now only larger than 4 standard deviations around the largest principal component. The factor $\sqrt{1+\sum\lambda^2}$ in the classical statistical interval formula [11] is ~ 40% lower compared to that of DB2 implying that the log-linear interval for the ITER prediction is significantly reduced. The ELMy H-mode data now satisfies the Kadomtsev constraint [9] - i.e., the scaling expression derived by log-linear regresion on this standard dataset is dimensionally correct - which was not the case with earlier versions of the dataset. The reasons why the Kadomtsev constraint is now satisfied, apparently as a result of the inclusion of the C-Mod data, is being investigated. One possibility is the reduction in the correlation between B and R. The new dataset is quite robust in the sense that the log-linear regression results and subsequent ITER predictions do not change appreciably if the dataset is perturbed. The Kadomtsev constrained ELMy H-mode log-linear scaling expression with the lowest RSME (15.64%) is obtained with the TAUC93 renormalisation [12]. This expression is given by (in units of s, MA, T, MW, 10^{19} m^{-3}, AMU, m, -, -):

$$\tau_{th}^{ELMy} = 0.0297\, I^{0.89}\, B^{0.18}\, P^{-0.64}\, n_{19}^{0.43}\, M^{0.13}\, R^{1.83}\, \varepsilon^{0.24}\, \kappa^{0.88} \qquad (4)$$

and is practically identical to the EPS97P(y) scaling [13]. It is equivalent to $\tau_{th}^{ELMy} \propto \tau_B\, \rho_*^{-0.98}\beta^{-0.50}\nu_*^{-0.10}$ i.e., a gyro-Bohm scaling. Comparing the H-mode (Eq. 4) and L-mode (Eq. 3) scalings, it is apparent that the H-mode enhancement factor will exhibit an inverse ρ_* scaling and therefore will tend to be larger for larger devices. The ITER prediction is 6.15 s. The scaling obtained without any renormalisation is $\propto \tau_B\, \rho_*^{-1.15}\beta^{-0.37}\nu_*^{-0.12}$ which predicts 7.08 s for ITER. It is the ASDEX corrections that make the β degradation stronger in Eq. (4) and reduce the $\rho*$ dependence which leads to the lower ITER prediction. The scaling is $\propto \tau_B\, \rho_*^{-0.68}\beta^{-0.50}\nu_*^{-0.12}$ if only the ASDEX corrections are applied and the prediction is 5.75 s for ITER. With the TAUC92 [10] or TAUC93 corrections applied only to the PDX data the scalings are $\propto \tau_B\, \rho_*^{-1.32}\beta^{-0.36}\nu_*^{-0.11}$ or $\propto \tau_B\, \rho_*^{-1.49}\beta^{-0.36}\nu_*^{-0.11}$, respectively, which thereby counteracts the ASDEX corrections on the $\rho*$ dependence. In [4] the equivalent of Eq.(4) using TAUC92 instead of TAUC93 can be found as well as fits using another definition of elongation, κ = area / (πa^2), which seems appropriate to use for the indented, bean shaped PBX-M and also START [14]. In [6] uncertainties of the exponents for the individual dimensionless physics variables have been estimated by a mapping of the RMSE minima from a series of constrained regressions. Two constraints are applied: the Kadomtsev constraint plus a constraint corresponding to a given value, y, of the exponent of one other dimensionless parameter. The 95% confidence interval $\pm\,\delta y$ can then be estimated from the plot of RMSE versus y. Typical values for δy are 0.27, 0.24 and 0.08 for ρ_*, β and ν_*, respectively.

Based on the log-linear models applied to various subsets of the data [4], the interval estimate for the ELMy H-mode confinement time in ITER is (4.4-6.8 s). This comes close to a classical statistical interval estimate based on the log-linear fit using TAUC92, allowing for a multiplication factor of 2 to roughly account for some of the modelling imperfections. Notice that scalings based on TAUC92 are slightly more conservative in the prediction for ITER than scalings based on TAUC93. Several non-linear scalings with lower RMSE's than that of the log-linear scalings have been found [4, 15, 16]. Allowing for these non-linear models, and a number of additional considerations as presented in [4], the 95% interval estimate is (3.5-8.0 s). Hence, in this case the (4.4-6.8 s) interval corresponds roughly to a 66% interval estimate, see Fig. 2.

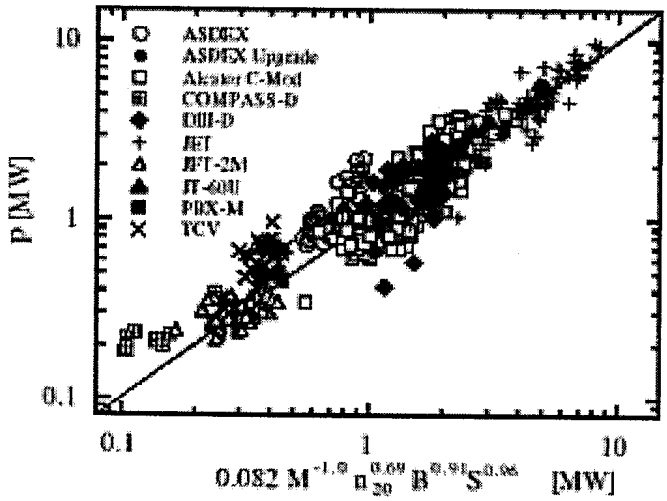

FIG. 1. Comparison of experimental power thresholds with scaling expression Eq.(1).

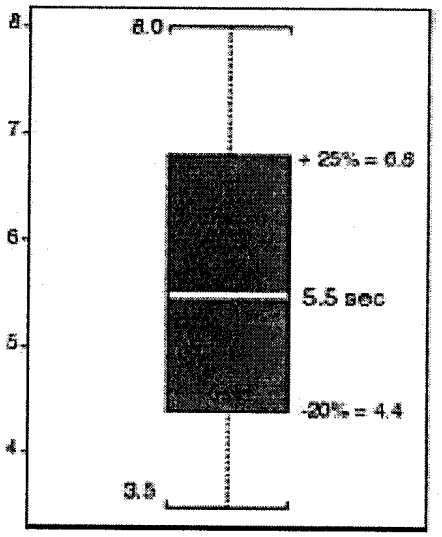

FIG. 2. Interval estimates of the confinement time in ITER at the standard operating point.

References

[1] RYTER, F., et. al., Nucl. Fusion 36 (1996) 1867.
[2] KAYE, S., et. al., Nucl. Fusion 37 (1997) 1303.
[3] THOMSEN, K., et. al., Nucl. Fusion 34 (1994) 131.
[4] "ITER Physics Basis" Chapter II, submitted to Nucl. Fusion (1998).
[5] MARTIN, Y., et. al., Proc. 25th Eur. Conf., Prague, 1998.
[6] VALOVIC, M. et. al., Proc. 25th Eur. Conf., Prague, 1998.
[7] ITER CONFINEMENT DATABASE AND MODELLING GROUP (presented by T. Takizuka), Fusion Energy 1996 (Proc 16th International Conference, Montreal, Canada), 2 (1996) 795.
[8] RIGHI, E., et. al., Submitted to Nucl. Fusion (1998).
[9] KADOMTSEV, B.B., Sov. J. Plasma Phys. 1 (1975) 295.
[10] ITER H-MODE DATABASE WORKING GROUP, (presented by O.J.W.F. Kardaun), Plasma Phys. Control. Nucl. Fus. Res. (Proc. 14th Int. Conf., Wurzburg, 1992), 3 (1993) 251.
[11] CHRISTIANSEN, J.P., et. al., Nucl. Fusion 32 (1992) 291.
[12] SCHISSEL, D.P., et. al., Proc. 20th Eur. Conf., Lisbon, 1993), Vol. 17C, Part I, 103.
[13] CORDEY, J.G., et. al., Plasma Phys and Control Fusion 39 (1997) B115.
[14] ROBINSON, D., et. al., To appear in Plasma Phys. Control. Fusion (1998).
[15] KARDAUN, O.J.W.F., et. al., Proc. 21st Eur. Conf., Montpellier, 1994), Vol. 18B, Part I, 90.
[16] TAKIZUKA, T., To appear in Plasma Phys. Control. Fusion.